Fracture of Interparticle MICP Bonds under Compression

Yang Xiao, M.ASCE[1]; Wentao Xiao, S.M.ASCE[2]; Huanran Wu[3]; Yi Liu, Ph.D.[4]; and Hanlong Liu, Ph.D.[5]

Abstract: Microbiologically induced calcium carbonate precipitation (MICP), as a promising reinforcement technique, has been investigated extensively through element and model tests. However, tests on the particle-scale behaviors of MICP bonds are rarely conducted yet, which constrains the development of constitutive and numerical models of MICP-treated sands. In this paper, a set of devices is designed to form MICP bonds between spherical quartz beads (SQBs) and spherical calcareous beads (SCBs) and investigate the microscopic compression behavior of the interparticle MICP bonds in comparison with portland cement (PC) bonds. The experimental results reveal that the PC bonds are the strongest, whereas the MICP bonds between SQB are the weakest. A higher cementation degree leads to higher strength and smaller dispersion among parallel specimens, while a larger interparticle distance causes smaller strength and greater dispersion. Identified with force–displacement curves and optical photos, the PC-treated SQB specimens are dominated by brittle failure, the MICP-treated SQB specimens can present ductile or brittle failure, and possible grain crushing is observed in the MICP-treated SCB specimens. Scanning electron microscopy (SEM) images suggest better interfacial bonding for the MICP-treated SCB specimens than for the MICP-treated SQB specimens. Gravity-related inhomogeneity is observed in the MICP bonds, whereas a homogeneous dense microstructure is observed in the PC bonds. **DOI: 10.1061/IJGNAI.GMENG-8282**.

Introduction

Microbiologically induced calcium carbonate precipitation (MICP) is a new microbial reinforcement technique in geotechnical engineering (DeJong et al. 2006; Whiffin et al. 2007; DeJong et al. 2010; Harkes et al. 2010; Al Qabany et al. 2012; Chu et al. 2012; Al Qabany and Soga 2013; He et al. 2020; Ma et al. 2022) and has been regarded as a green reinforcement technique with broad prospects (Whiffin et al. 2007; DeJong et al. 2010; Consoli et al. 2012; DeJong et al. 2013; Rahmannejad and Toufigh 2018; Irani and Ghasemi 2021; Xiao et al. 2022b). The urease-producing bacteria are widely used as the active bacteria in the MICP technique, and the biochemical reaction process is summarized as follows (Whiffin et al. 2007; Mortensen et al. 2011; Zhao et al. 2014; Cheng et al. 2019): $NH_2–CO–NH_2 + 2H_2O \rightarrow 2NH_4^+ + CO_3^{2-}$, and $Ca^{2+} + CO_3^{2-} \rightarrow CaCO_3\downarrow$. Generally, the cementing mechanism of MICP is different from traditional cementing materials, such as portland cement (PC), lime, asphalt, and resin (Consoli et al. 2012; Toohey et al. 2013; Wang et al. 2019a, e). $CaCO_3$ crystals can form effective cementation among soil particles to improve the physical and mechanical properties of soils, such as increasing unconfined compressive strength (Cheng et al. 2013; Chu et al. 2014; Soon et al. 2014; Venda Oliveira et al. 2015; Liu et al. 2019; Wen et al. 2019; Xiao et al. 2019b; Pan et al. 2020; Sharma et al. 2021; Sun et al. 2021b), splitting tensile strength (Venda Oliveira et al. 2015; Nafisi et al. 2019; Xiao et al. 2019b; Ahenkorah et al. 2020), shear strength (Montoya and DeJong 2015; Gao et al. 2019) and liquefaction resistance (Sasaki and Kuwano 2016; Feng and Montoya 2017; Xiao et al. 2018, 2019a; Zamani and Montoya 2019; Riveros and Sadrekarimi 2020; Mousavi and Ghayoomi 2021; Sun et al. 2021a; Lee et al. 2022), reducing compressibility (Lee et al. 2013; Lin et al. 2016; Cardoso et al. 2018; Gao et al. 2019; Montoya et al. 2019; Xiao et al. 2021d) and particle breakage (Xiao et al. 2020a), decreasing permeability (Chu et al. 2013; Martinez et al. 2013; Soon et al. 2014; Proto et al. 2016; Jiang and Soga 2017; Pham et al. 2018; Montoya et al. 2019; Yang et al. 2019; Ma et al. 2021; Montoya et al. 2021), increasing thermal conductivity (Venuleo et al. 2016; Martinez et al. 2019; Wang et al. 2020; Xiao et al. 2021b), and improving erosion resistance (Adams et al. 2013; Jiang and Soga 2017; Jiang et al. 2017; Wang et al. 2018; Jiang et al. 2019; Fattahi et al. 2020; Liu and Gao 2020; Liu et al. 2021; Xiao et al. 2022c, e). In addition, a large number of physical model tests (van Paassen et al. 2010b; Montoya et al. 2013; Gomez et al. 2017, 2018; Nassar et al. 2018; Darby et al. 2019; San Pablo et al. 2020; Xiao et al. 2020b, 2022d; Zamani et al. 2021) and field pilot trials (Gomez et al. 2015; Xiao et al. 2022e) have shown that the strength of solidified soil is closely related to the $CaCO_3$ content. The higher the $CaCO_3$ content, the better the macroscopic mechanical properties of the MICP-treated samples (Gomez et al. 2017; Cheng et al. 2019; Xiao et al. 2019c). Furthermore, detailed microstructural observations with scanning electron microscopy (SEM) (Whiffin et al. 2007; DeJong et al. 2010; van Paassen et al. 2010a; Terzis and Laloui 2019; Xiao et al. 2019b) and X-ray computed tomography (Dadda et al. 2017, 2019; Mahawish et al. 2019) have revealed that the mechanical properties of MICP-treated sands are mainly controlled by the effective cementation between particles. A series of microfluidic tests have been conducted to observe the in situ deposition of

[1]Professor, Key Laboratory of New Technology for Construction of Cities in Mountain Area, State Key Laboratory of Coal Mine Disaster Dynamics and Control, School of Civil Engineering, Chongqing Univ., Chongqing 400045, China. Email: hhuxyanson@163.com

[2]Master's Candidate, School of Civil Engineering, Chongqing Univ., Chongqing 400045, China. Email: xwtcwmcq@163.com

[3]Assistant Professor, School of Civil Engineering, Chongqing Univ., Chongqing 400045, China (corresponding author). Email: hwucqu@163.com

[4]State Key Laboratory of Hydraulics and Mountain River Engineering, College of Water Resource and Hydropower, Sichuan Univ., Chengdu 610065, China. Email: liuyi616@scu.edu.cn

[5]Professor and Vice President, School of Civil Engineering, Chongqing Univ., Chongqing 400450, China. Email: cehliu@cqu.edu.cn

Note. This manuscript was submitted on August 3, 2022; approved on October 14, 2022; published online on December 27, 2022. Discussion period open until May 27, 2023; separate discussions must be submitted for individual papers. This paper is part of the ***International Journal of Geomechanics***, © ASCE, ISSN 1532-3641.

$CaCO_3$ in porous media in real time (Wang et al. 2019c, d, 2021; Xiao et al. 2021a, 2022a). Moreover, theoretical and numerical investigations have also been conducted to further investigate the particle-scale cementing mechanism and its effects on the macroscopic mechanical properties of MICP-treated sands. Based on thermodynamics, Xiao et al. (2021c) developed a constitutive model for MICP-treated sands to capture the effects of biocementation and its microstructural degradation on the static and dynamic mechanical responses. In recognition of the multiscale nature of cemented and uncemented sands, discrete element method (DEM) (Cundall and Strack 1979; Wang and Leung 2008) and continuum–discrete coupled multiscale methods (Wu et al. 2018; Liang and Zhao 2019; Kularathna et al. 2021; Zhao et al. 2021, 2022) have been widely used to investigate the microscopic mechanisms of macroscopic mechanical properties. As the key components of DEM, the mechanical characteristics of the interparticle contacts and cementations have drawn much attention. Therefore, Jiang et al. (2012) have specifically designed experimental instruments to investigate the mechanical characteristics of contacts and cementations between particles (Jiang et al. 2013). Besides, Wang et al. (2017) conducted a series of uniaxial compression and shear tests on artificially cemented sand particles, proposed three failure modes, and emphasized the influence of contact morphology (Wang et al. 2019b). Recently, Ren et al. (2021) carried out tensile and monotonic shear tests of interparticle $CaCO_3$ bonds using chemical solutions. Ham et al. (2022) investigated the tensile and shear strength of MICP bonds with grain-scale experiments. However, the compressive characteristics of MICP bonds are rarely investigated with experiments at the grain scale yet. In this study, a set of devices is specifically designed, consisting of a compression loading device and a high-definition digital camera, to achieve in situ observation of the compression failure process of interparticle MICP bonds. Effects of granular material, cementing material, interparticle distance, and cementation degree on the compressive strength and failure mode of the interparticle bonds are explored. The grain-scale compressive mechanical characteristics of interparticle MICP bonds in this study lay a microscopic mechanical foundation for the multiscale constitutive modeling and numerical simulation of MICP-treated sands.

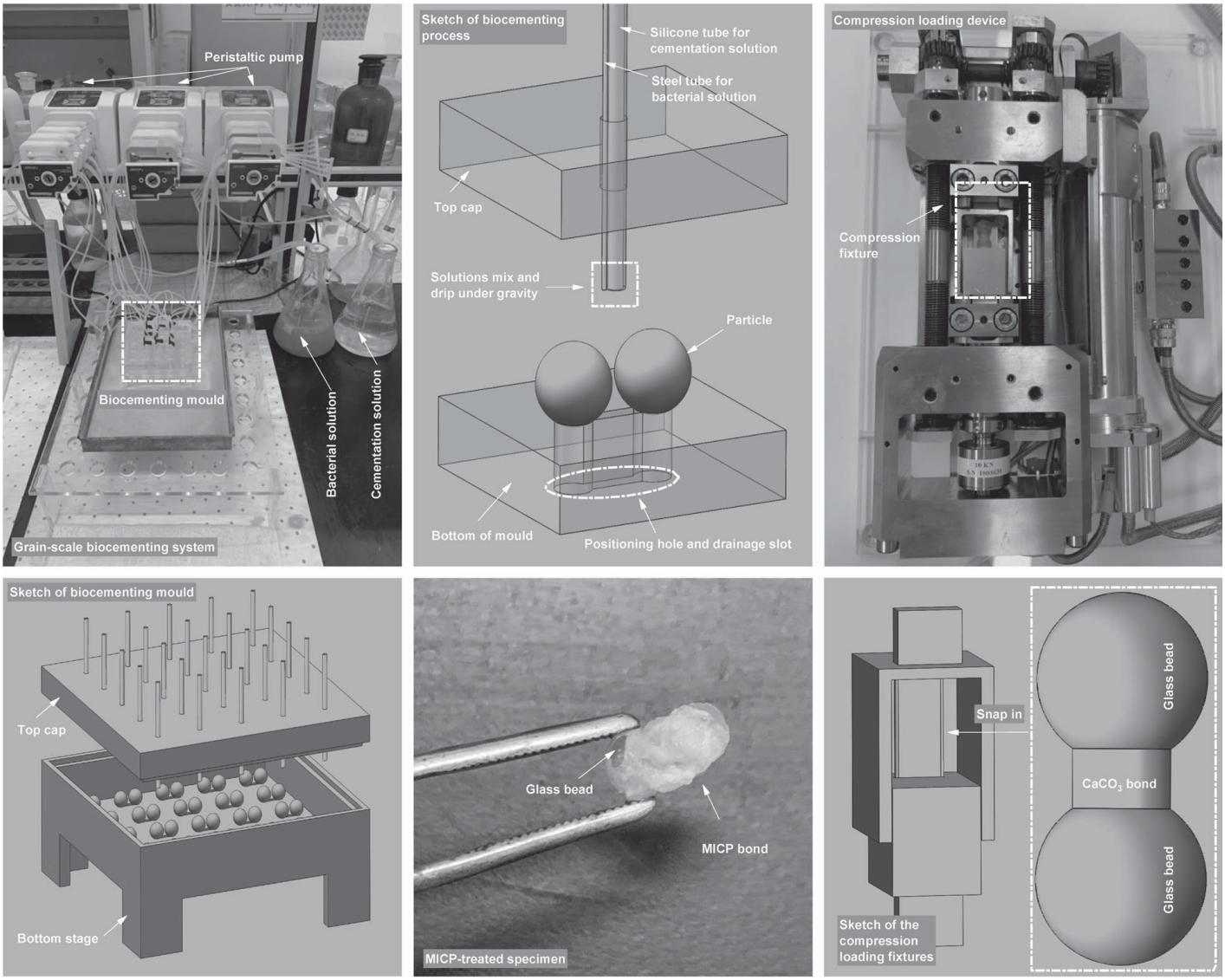

Fig. 1. Preparation of the MICP-treated specimens composed of two particles in the biocementing mold through the mixture of the cementation solution from the silicone tube and bacteria solution from the steel tube, and the grain-scale loading device for cemented specimens.

Experimental Details and Testing Procedures

The particle-scale mechanical characteristics of interparticle biocementation are likely affected by the properties of particulate materials. Quartz and calcareous sands are the two common materials encountered in the MICP treatment (Cui et al. 2017; Liu et al. 2019; Xiao et al. 2022d). Given the great impact of particle shape on the mechanical responses (Xiao et al. 2019c, d), spherical quartz beads (SQBs, i.e., glass beads from BKMAM, Changde, Hunan) and spherical calcareous beads (SCBs, i.e., homemade natural coral sands from the South China Sea) are adopted as the particles for cementation. A diameter of 6 mm is adopted for all the beads to eliminate the effect of particle size. The spherical beads are cleaned and oven-dried before the experiments. The diameter of the bead is measured with a micrometer with an accuracy of 0.001 mm, and the mass is weighed with an analytical balance with an accuracy of 0.001 g before cementation. MICP-treated two-particle specimens were prepared with a homemade grain-scale biocementing system. The sketch of the biocementing mold and the detailed sketch of the biocementing process are shown in Fig. 1. The holes in the top cap of the mold were used to fix the pipes for transporting the bacterial and the cementation solutions. The bottom stage of the mold contained positioning holes in pairs to control the positions of the particles and drainage slots connecting the holes to discharge excess solutions. The holes in the top cap were in the middle of the corresponding pairs in the bottom stage to ensure that the solutions drip to the center of the two particles. Moreover, the bacterial and cementation solutions were transported through two pipes and mixed right before dripping, which can prevent pipe clogging by $CaCO_3$ effectively. A peristaltic pump was used to pump the solutions in the pipes at constant rates. The ratio between the rates of the two solutions was 1:4, with 7.33 μL/min for the bacterial solution and 29.33 μL/min for the cementation solution. *Sporosarcina pasteurii* was adopted as the active bacteria (Xiao et al. 2022a), which can hydrolyze urea quickly. The activated bacterial solution and sterilized glycerol aqueous solution with a volume concentration of 80% were mixed with a mix ratio of 4:1 and then frozen to −80°C to maintain the integrity of the solution. For MICP treatment, 1-mL of unfrozen glycerol bacterial solution was inoculated into 500-mL of liquid culture medium and then placed into a shaking incubator at 30°C for propagation at a constant shaking rate of 200 rpm for 24 h. The liquid culture

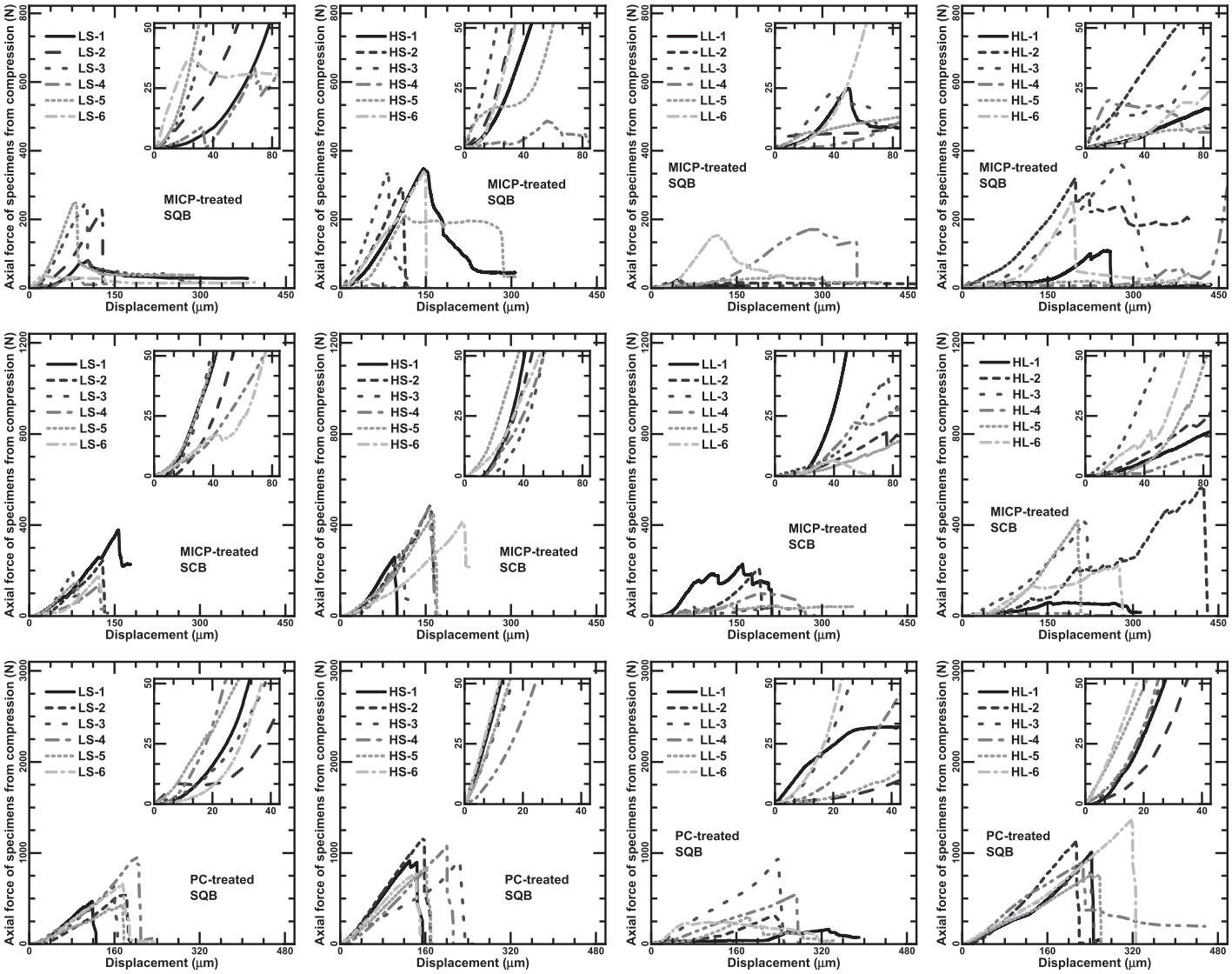

Fig. 2. Relationship between the axial force and the displacement for the MICP-treated SQB, MICP-treated SCB, and PC-treated SQB specimens with different treatment levels and different interparticle distances under grain-scale compression loading.

medium consisted of 20 g/L yeast extract, 10 g/L NH_4Cl, 12 mg/L $MnCl_2 \cdot H_2O$, and 24 mg/L $NiCl_2 \cdot 6H_2O$ (Xiao et al. 2019b). The pH was adjusted to 9.2 with 1 M NaOH solution. The average urease activity of the final bacterial solution was 1.65 mM/min. The cementation solution consisted of 0.5 mol/L calcium chloride ($CaCl_2$) and 0.5 mol/L urea. The distance between the particles was controlled to be either 1 or 2 mm. The cementation degree was controlled through time for pumping (24 h for the low cementation degree and 48 h for the high cementation degree). Thereafter, the MICP-treated specimens were placed into deionized water and cured for 24 h with the cementation mold. After the initial curing, the MICP-treated specimens were taken out from the mold and soaked into deionized water for another 48 h to further remove the remnant $CaCl_2$ and other salts. Then, the specimens were oven-dried and weighed to calculate the content of $CaCO_3$. Notably, the $CaCO_3$ content might be apparently larger than element specimens due to the intention to form effective bonds between two apart particles. Considering the erratic shape of the biocementation, as shown in Fig. 1, the diameters of the cementation were measured along three different directions with a micrometer. The mean of the three measurements was regarded as the equivalent diameter and then used to estimate the cross-sectional area, which can be adopted to further calculate the strength of the biocementation. Besides MICP, PC was used to bond SQB, serving as a control group. The cement slurry was prepared using a water–cement weight ratio of 0.6. The interparticle cementation was prepared with a silicone tube of 10 mm in length. The inner diameter of the tube is 4 mm for the low cementation degree and 5 mm for the high cementation degree, respectively. A quartz bead was clamped to one end of the silicone tube, and the cement slurry was filled into the tube from the other end, which would be sealed by the second quartz bead thereafter. The specific distance between the two particles by PC treatment is the same as that by MICP treatment. The silicone tube was removed after setting it for 3 days. Then, the specimens were immersed in deionized water and cured for 28 days. The final specimens were oven-dried and weighed, and the diameters of the cementation were measured along two different directions with a micrometer. As shown in Fig. 1, a particle-scale loading device (Tensile & Compression Module, Schwerte, Germany) with a set of fixtures was designed for the compression tests on the bonded two-particle specimens, considering the particular size and shape of the specimen. The measuring range of the

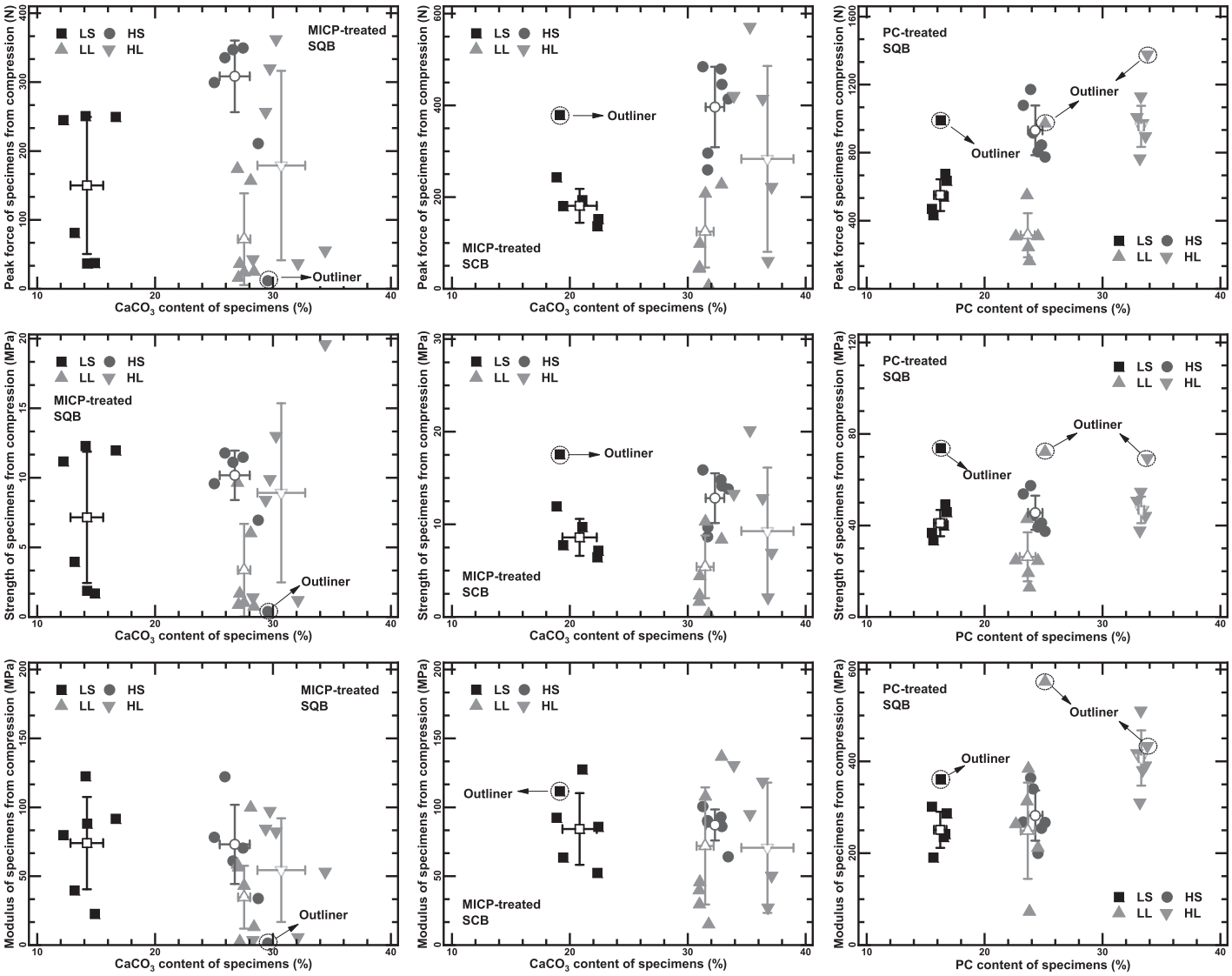

Fig. 3. Variations of the peak force, strength, and secant modulus with the cementation level for the MICP-treated SQB, MICP-treated SCB, and PC-treated SQB specimens with different treatment levels and different interparticle distances.

compression force sensor is 10 kN, and the acquisition accuracy is 0.1 N. Displacement-controlled loading was adopted with a loading rate of 0.1 μm/s. The deformation process of the specimen, including the initiation and the development of the cracks, was in situ recorded with a full-frame digital camera (Nikon D810, Tokyo, Japan). After the compression tests, some representative specimens, including particles, interparticle bonds, and particle–bond interfaces, were observed by the SEM instrument (Waltham, Massachusetts) to examine the detailed microstructure. In this study, a series of particle-scale compression tests were organized into four MICP-treated SQB, four MICP-treated SCB, and four PC-treated SQB groups with two cementation levels and two interparticle distances. Parallel specimens are prepared to ensure six sets of valid data considering the dispersion.

Experimental Results and Discussions

Fig. 2 shows the force–displacement curves of MICP-treated SQB, MICP-treated SCB, and PC-treated SQB specimens of different cementation levels and interparticle distances under axial compression, respectively. For the symbols in the legend, that is, "LS-*x*," "HS-*x*," "LL-*x*," and "HL-*x*," the first capital letter, "L" and "H" represent low and high cementation degree, respectively; the second capital letter "S" and "L" represent small (i.e., 1 mm) and large interparticle distance (i.e., 2 mm), respectively; and the third letter represents the number of tests. Largely similar mechanical responses are observed for the three groups of specimens (i.e., MICP-treated SQB, MICP-treated SCB, and PC-treated SQB specimens with different cementation levels and interparticle distances), showing gradual increases in stiffness to constant values at the prepeak stages and abrupt force drops at the postpeak stages. The gradual increase in stiffness is corresponding to the Hertz-type contacts (Johnson et al. 1971) between the particles and the loading fixture, while the force drop is caused by the failure of the interparticle bond. Besides, the average peak force of the three groups of specimens with low cementation and large interparticle distance is smaller than others. The mechanical responses of the specimens might be influenced by both the particulate material and the cementation material. More apparent dispersion of the experimental results is noted for MICP-treated SQB specimens compared with MICP-treated SCB specimens with different granular materials,

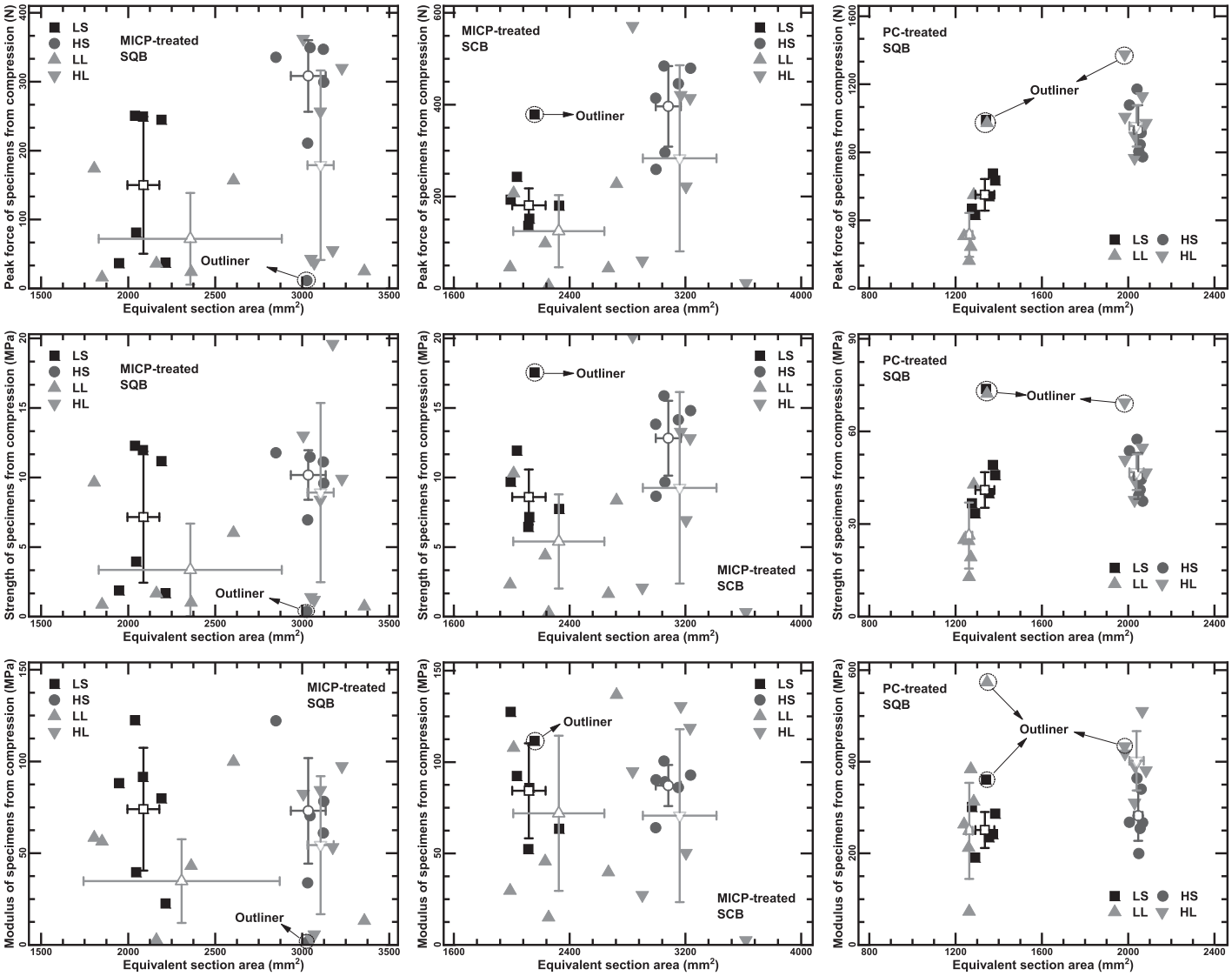

Fig. 4. Variations of the peak force, strength, and secant modulus with the equivalent section area for the MICP-treated SQB, MICP-treated SCB, and PC-treated SQB specimens with different treatment levels and different interparticle distances.

and PC-treated SQB specimens with different cementation materials. Furthermore, MICP-treated SCB specimens show higher stiffness and peak force and less ineffective bonds than MICP-treated SQB specimens. This is possibly caused by the better interfacial compatibility between MICP cementation and SCB due to the similar components, which will be discussed in detail later. Given the use of silicone tubes as molds to constrain the shape of interparticle bonds in PC-treated SQB specimens, the portion of ineffective bonds is much smaller. PC-treated SQB specimens have notably larger peak force (with maximum peaks greater than 1,000 N) than MICP-treated SQB specimens (with maximum peaks around 400 N) and SCB specimens (with maximum peaks around 600 N). Considering the large dispersion of the experimental data and the limited number of parallel tests, scatter plots with error bars are presented to illustrate the relations of the peak force, the strength, and the secant modulus at peak force with $CaCO_3$ content and equivalent section area (Figs. 3 and 4). Although several specimens are described as ineffective bonds based on the peak forces, bias might be caused if we simply remove these data from the dataset. On the other hand, outliers in terms of peak forces are identified following the $1.5I_{QR}$ rule, in which they are defined as data points more than 1.5 times the interquartile range ($I_{QR} = Q_3 - Q_1$, where Q_1 is the first quartile and Q_3 is the third quartile) beyond the quartiles (Q_1 and Q_3). Five outliers are identified in this way, namely, MICP-treated SQB specimen (HS-4), MICP-treated SCB specimen (LS-1), and PC-treated SQB specimens (LS-4, LL-3, and HL-6), with at least five remnants in each group. The mean values and the standard deviation for the error bars are calculated, excluding those outliers. It can be seen from Figs. 3 and 4 that the peak force of MICP-treated SQB specimens increases apparently from low cementation to high cementation with the increases in $CaCO_3$ content and equivalent section area for both interparticle distances of 1 and 2 mm. The average peak force of specimens with an interparticle distance of 1 mm is 312 N for the high cementation group and 158 N for the low cementation group. Comparatively, the average peak force of specimens with a distance of 2 mm is 187 N for the high cementation group and 72 N for the low cementation group. The increase in interparticle distance decreases the peak force apparently, and this decrease is more significant for the low cementation group. Specifically, Group LL of MICP-treated SQB specimens presents small strength with similar $CaCO_3$ content but dispersive equivalent section area, suggesting

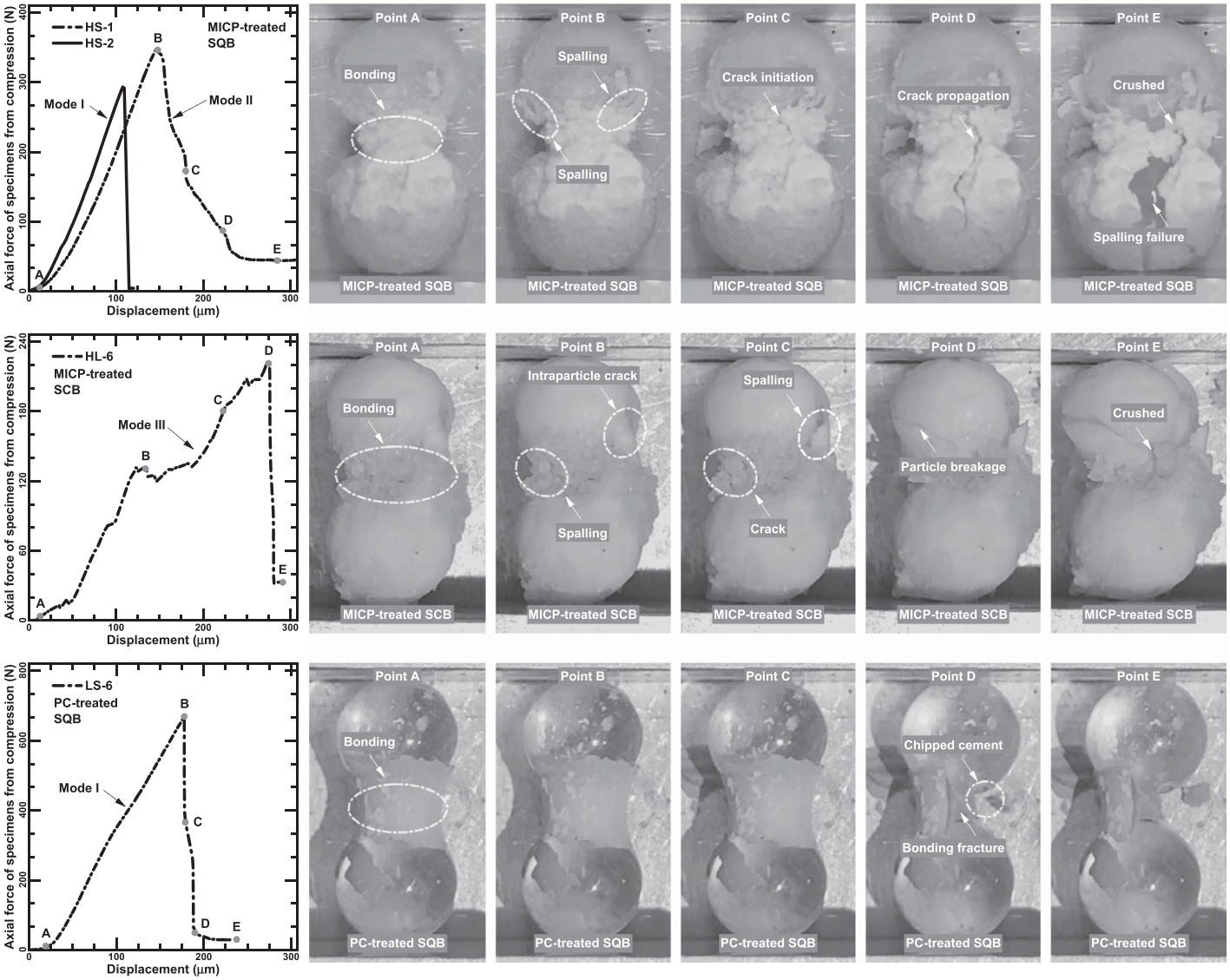

Fig. 5. Typical axial force–displacement curves and failure processes with crack propagation various failure modes for the MICP-treated SQB, MICP-treated SCB, and PC-treated SQB specimens with different treatment levels and different interparticle distances.

great dispersion in the internal structure of the MICP bonds. It is interesting to note that the strength and the secant modulus for Groups LS, HS, and HL are in the same range, although the lower cementation degree and larger interparticle distance increase the intragroup dispersion with more ineffective interparticle bonds. Figs. 3 and 4 also display the peak force, the strength, and the secant modulus versus the $CaCO_3$ content and the equivalent section area for the MICP-treated SCB specimens, respectively. In general, the mechanical responses of MICP-treated SCB specimens are qualitatively similar to those of MICP-treated SQB specimens, while the peak force, the strength, and the modulus of MICP-treated SCB specimens are all larger. Similar to the MICP-treated SQB specimens, the peak force for both interparticle distances increases apparently with the increase in cementation degree. The average peak force of specimens with 1-mm interparticle distance is 396 N for the high cementation degree, whereas 181-N for the low cementation degree. For those with 2-mm interparticle distance, the average peak force is 283 and 105-N for the high and low cementation degrees, respectively. Notably, the equivalent section area increases with the cementation degree as well, which diminishes the differences in strength. Moreover, the average strength and the average secant modulus decrease mildly with the increase in the interparticle distance, although both $CaCO_3$ content and equivalent section area increase, which might be a potential cause of the weaker specimen with higher porosity (Zamani and Montoya 2018; Xiao et al. 2021d). Notably, as shown in Figs. 3 and 4, the dispersion of the data points for the PC-treated SQB specimens is significantly smaller than that for MICP-treated specimens and the dispersion does not vary apparently with the interparticle distance due to the well-controlled mold. Similar to those MICP-cemented specimens, the increase in cementation degree leads to higher peak force for both interparticle distances of 1 and 2 mm. However, the differences in peak forces are diminished by the corresponding increase in section area, leading to closer strength for the four groups. As to the secant modulus, the average values for Groups LS, HS, and LL are similar, while that for Group HL is slightly larger possibly due to the combining effects of bond thickness and diameter considering the limited dispersion of the data.

Fig. 5 shows two typical force–displacement curves for MICP-treated SQB specimens, characterized by Mode I and Mode II

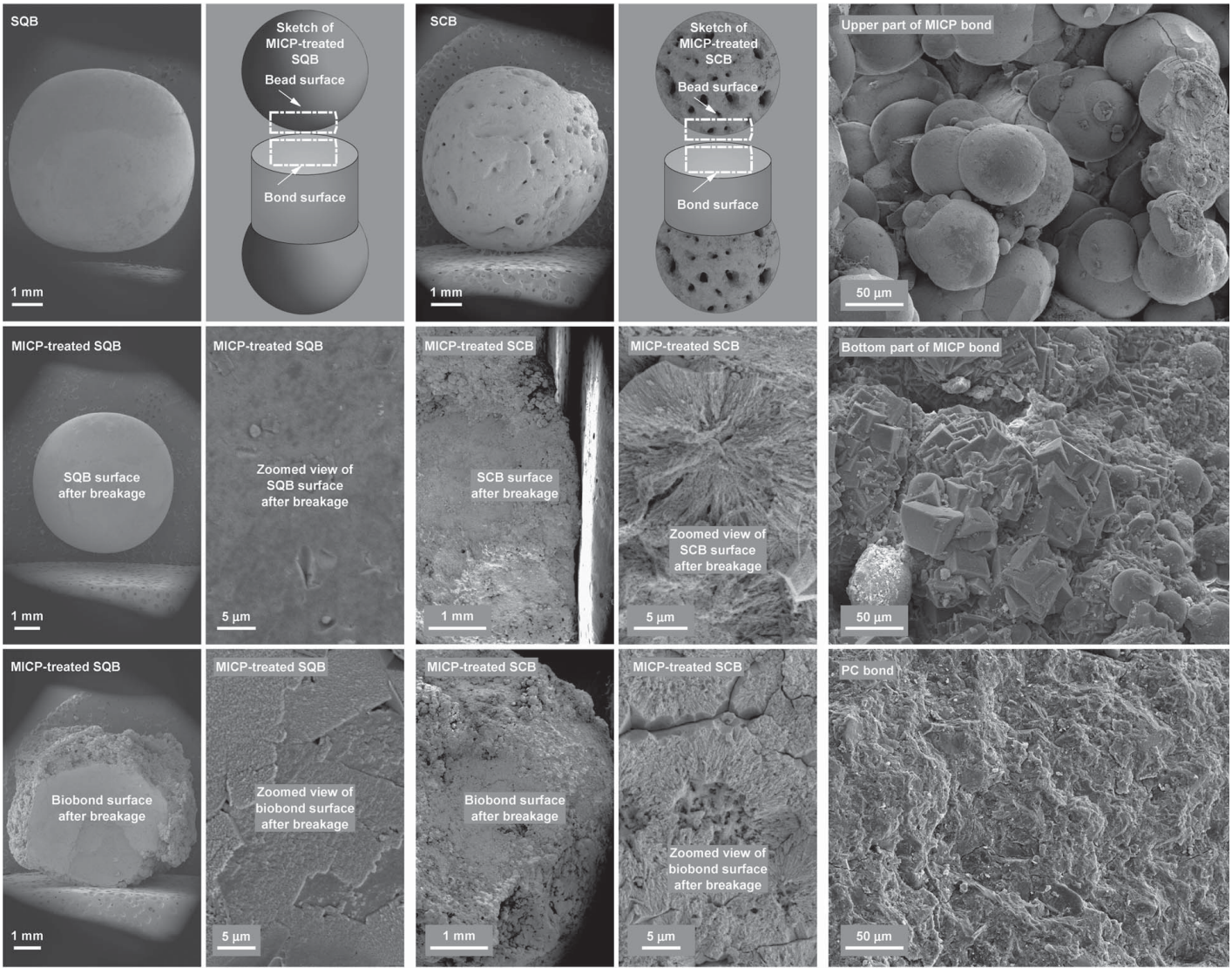

(a) (b) (c)

Fig. 6. SEM images from sketch of cemented specimens: (a) postfailure interfacial characteristics of the MICP-treated SQB specimens; (b) postfailure interfacial characteristics of the MICP-treated SCB specimens; and (c) upper and bottom parts of MICP bond and PC bond.

failure. The prepeak behaviors for the two failure modes are qualitatively similar, presenting increasing stiffness, which is consistent with the Hertz contact theory (Johnson et al. 1971). As to the postpeak responses, Mode I failure represents a rather brittle behavior, characterized by a sharp force drop after the peak without apparent residual strength. On the contrary, Mode II failure represents a ductile response, featured by a gradual reduction in force at the postpeak stage. The right optical photos present the typical failure process of Mode II specimens. The specimens are first compacted under axial load, presenting no apparent change on the surface of the cementation (Point A). At the force peak, spalling is observed between the quartz beads and the MICP cementation at its margin, while the main body of the cementation remains intact (Point B). With the further increase in axial displacement, a clear crack begins to initiate from one side of the interparticle bond (Point C) and penetrates through the entire bond (Point D), accompanying the continuous decrease in axial force. The cementation is finally crushed into pieces with marginal residual strength (Point E). It is noteworthy that the failure processes observed from optical photos are similar for the Mode I failure, except that the force–displacement curves present no residual strength at the postpeak stage. For MICP-treated SCB specimens in Fig. 5, some of them show the same failure modes (Modes I and II) as the MICP-treated SQB ones, while a different failure mode (Mode III) accompanied by apparent particle breakage is also observed. The force–displacement curve for Mode III failure presents an unsteady increase in force with an axial displacement, which can be characterized into three stages, that is, an initial increase in axial force (Stage a: 0→B), followed by a plateau stage and the second increase in axial force (Stage b: B→D), and the apparent postpeak force drop (Stage c: D→E). In terms of the failure process of the specimen, spalling is observed at the end of Stage a (Point B), similar to the pattern at the force peak of Modes I and II specimens. A minor intraparticle crack begins to appear with the further increase in axial force during Stage b (Point C) with the initiation of a major crack at the force peak (Point D). The postpeak force drop is accompanied by the overall breakage of SCB into pieces (Point E). As to PC-treated SQB specimens in Fig. 5, most of them present Mode I failure with rather brittle mechanical responses and no residual strength. Compared with MICP-treated SQB specimens, the failure of PC-treated specimens under compression is more sudden and brittle. No visible cracks are observed at the force peak (Point B), and the failure of the interparticle bond is characterized by a sudden crack and the burst of bond fragments, accompanied by the abrupt force drop (Points C and D). The sudden brittle failure of the cement bonds is in line with the unconfined mechanical responses of brittle rock and strong cement. The difference between PC-treated and MICP-treated specimens is caused by the cementing materials, which suggests that the compressive strength and the brittleness of the portland cement in this study are much higher than their counterparts of $CaCO_3$ produced by MICP. The MICP-treated SCB specimens present higher strength and stiffness than the MICP-treated SQB ones, which is mainly caused by the different material properties of the particles. While optical photos have been used to observe the failure process, SEM photos are adopted to analyze the detailed mechanisms. The SQB presents a smooth surface without intraparticle pores [Fig. 6(a)], whereas the SCB has a relatively rough surface with intraparticle pores [Fig. 6(b)]. Besides, the chemical composition of SCB is $CaCO_3$, the same as that of MICP bonds, while that of SQB is SiO_2. The internal pores and the chemical composition of $CaCO_3$ lead to lower particle strength of the SCB (Stocks-Fischer et al. 1999; Coop et al. 2004), which is responsible for the particle breakage of SCB in the Mode III failure. The rougher surface and the same chemical composition as the cementation may influence the interfacial characteristics. The postfailure particle–cementation interfaces are presented in Figs. 6(a and b) for MICP-treated SQB and SCB samples, respectively. The surface of the SCB after breakage is covered by lots of remnant $CaCO_3$, and that of the SQB after breakage is smooth, similar to that of the pretreated SQB. Moreover, the zoomed views of the particle side and the cementation side for the MICP-treated SQB specimens show smooth surfaces with marginal defects, suggesting an adhesive failure (Bennett et al. 1974). On the contrary, the zoomed views of MICP-treated SCB specimens present radial textures on both sides, matching each other, suggesting a cohesive failure near the interface (Bennett et al. 1974; Ren et al. 2021). The difference in fracture types between MICP-treated SQB and SCB specimens suggests better interfacial bonding between the MICP cementation and the SCB, which may cause the higher strength and stiffness of MICP-treated SCB specimens as compared with the MICP-treated SQB ones. The PC-treated SQB specimens present much higher strength and stiffness than the MICP-treated ones, attributed to the different cementing materials. Microstructural features of MICP and PC bonds are observed with SEM [Fig. 6(c)]. It is interesting to observe the different features of $CaCO_3$ at the upper and the bottom parts of the MICP bond formed following the dripping method. The upper part of the MICP bond consists of loosely packed spherical $CaCO_3$ crystals. In contrast, the $CaCO_3$ at the bottom is relatively dense, with no apparent pores, and most of the crystals are in the form of densely packed rhombohedral crystals, with minor spherical crystals. As compared with MICP bonds, the microstructure of PC bonds is relatively homogeneous, with no apparent pores.

Conclusions and Remarks

Compression tests are conducted on cemented two-particle specimens to investigate the effects of cementing material, particle material, cementation degree, and interparticle distance on the particle-scale compression behavior of MICP bonds between spherical particles. The failure process is recorded with a high-definition digital camera, and the failure mechanism is analyzed with SEM photos. The compression behavior of the cemented two-particle specimen is affected by both the cementing material and the particle material. Generally, the PC-treated specimens are stronger than those MICP-treated ones, and the MICP bonds between SQBs are weaker than those between SCBs. The compression behavior of MICP bonds is significantly affected by the cementation degree and the interparticle distance. Higher cementation degrees and smaller interparticle distances lead to higher strength of the MICP bonds. The increase in interparticle distance and the decrease in cementation degree cause larger dispersion among parallel specimens and more ineffective interparticle bonds. Mode I failure with brittle response and abrupt force drop is the dominating failure mode of PC-treated SQB specimens. Mode II failure with ductile response and gradual reduction in force at the postpeak stage is also observed, besides Mode I failure, for MICP-treated SQB specimens. The failure mode of MICP-treated SCB specimens is the most complex, with possible Mode III failure accompanied by particle crushing. SEM images indicate that the debonding in the MICP-treated SQB specimens is an adhesive failure while that in the MICP-treated SCB specimens is a cohesive failure, suggesting better interfacial bonding between the MICP bond and the SCB, which may cause the higher strength and stiffness of MICP-treated SCB specimens over MICP-treated SQB ones. The microstructure of the PC bond is more homogeneous with no apparent pores, whereas the MICP bond presents apparent inhomogeneity under gravity with loosely packed spherical crystals in the upper part and densely

packed rhombohedral crystals in the bottom of the bond. The above findings would help to explain the effects of porosity, cementation degree, cementing material, and particle material on the macroscopic mechanical responses, and serve as a valuable reference for the precise establishment of multiscale constitutive theory and the elaborate development of the DEM model for capturing failure of MICP-treated soils. Nevertheless, the particle-scale mechanical characteristics of MICP bonds are multifold, including the responses under compression, tension, shearing, rolling, and their hybrids. The limited dataset of compressive characteristics of MICP bonds under well-controlled testing conditions in this study is a good start but not enough for a quantitative basis. More particle-scale mechanical tests under more complex MICP treatment conditions and loading conditions are necessary.

Data Availability Statement

All data, models, and codes generated or used during the study appear in the published article. The optical images and recorded videos of the compression tests of biotreated sand specimens, the SEM images of other biotreated specimens, and additional data for possible discussions and comparisons are available from the corresponding author upon reasonable request.

Acknowledgments

The study was financially supported by the National Natural Science Foundation of China (Grant Nos. 52108303, 51922024, 52078085, and 41831282) and Chongqing Talents Program (Grant No. cstc2021ycjh-bgzxm0051). Huanran Wu acknowledges the support from the China Postdoctoral Science Foundation (Grant No. 2021M693741) and the Natural Science Foundation of Chongqing, China (Grant No. cstc2020jcyj-bshX0111). The authors thank Mr. H. H. Zhao for the assistance in the specimen preparation and the mechanical experiments, and Dr. X. He, Dr. J. Q. Shi, and Mr. G. L. Ma for their suggestions on the analyses of MICP reinforcement mechanisms. Finally, special thanks to the Analytical and Testing Center of Chongqing University for the instruments used in this study.

References

Adams, B. T., M. Xiao, and A. Wright. 2013. "Erosion mechanisms of organic soil and bioabatement of piping erosion of sand." *J. Geotech. Geoenviron. Eng.* 139 (8): 1360–1368. https://doi.org/10.1061/(ASCE)GT.1943-5606.0000863.

Ahenkorah, I., M. M. Rahman, M. R. Karim, and P. R. Teasdale. 2020. "A comparison of mechanical responses for microbial- and enzyme-induced cemented sand." *Geotech. Lett.* 10 (4): 559–567. https://doi.org/10.1680/jgele.20.00061.

Al Qabany, A., and K. Soga. 2013. "Effect of chemical treatment used in MICP on engineering properties of cemented soils." *Géotechnique* 63 (4): 331–339. https://doi.org/10.1680/geot.SIP13.P.022.

Al Qabany, A., K. Soga, and C. Santamarina. 2012. "Factors affecting efficiency of microbially induced calcite precipitation." *J. Geotech. Geoenviron. Eng.* 138 (8): 992–1001. https://doi.org/10.1061/(ASCE)GT.1943-5606.0000666.

Bennett, S. J., K. L. Devries, and M. L. Williams. 1974. "Adhesive fracture mechanics." *Int. J. Fracture* 10 (1): 33–43. https://doi.org/10.1007/BF00955077.

Cardoso, R., I. Pires, S. O. D. Duarte, and G. A. Monteiro. 2018. "Effects of clay's chemical interactions on biocementation." *Appl. Clay Sci.* 156: 96–103. https://doi.org/10.1016/j.clay.2018.01.035.

Cheng, L., R. Cord-Ruwisch, and M. A. Shahin. 2013. "Cementation of sand soil by microbially induced calcite precipitation at various degrees of saturation." *Can. Geotech. J.* 50 (1): 81–90. https://doi.org/10.1139/cgj-2012-0023.

Cheng, L., M. A. Shahin, and J. Chu. 2019. "Soil bio-cementation using a new one-phase low-pH injection method." *Acta Geotech.* 14 (3): 615–626. https://doi.org/10.1007/s11440-018-0738-2.

Chu, J., V. Ivanov, M. Naeimi, V. Stabnikov, and B. Li. 2013. "Microbial method for construction of an aquaculture pond in sand." *Géotechnique* 63 (10): 871–875. https://doi.org/10.1680/geot.SIP13.P.007.

Chu, J., V. Ivanov, M. Naeimi, V. Stabnikov, and H.-L. Liu. 2014. "Optimization of calcium-based bioclogging and biocementation of sand." *Acta Geotech.* 9 (2): 277–285. https://doi.org/10.1007/s11440-013-0278-8.

Chu, J., V. Stabnikov, and V. Ivanov. 2012. "Microbially induced calcium carbonate precipitation on surface or in the bulk of soil." *Geomicrobiol. J.* 29 (6): 544–549. https://doi.org/10.1080/01490451.2011.592929.

Consoli, N. C., R. C. Cruz, B. S. Consoli, and S. Maghous. 2012. "Failure envelope of artificially cemented sand." *Géotechnique* 62 (6): 543–547. https://doi.org/10.1680/geot.11.P.037.

Coop, M. R., K. K. Sorensen, T. Bodas Freitas, and G. Georgoutsos. 2004. "Particle breakage during shearing of a carbonate sand." *Geotechnique* 54 (3): 157–163. https://doi.org/10.1680/geot.2004.54.3.157.

Cui, M., J. Zheng, R. Zhang, H. Lai, and J. Zhang. 2017. "Influence of cementation level on the strength behaviour of bio-cemented sand." *Acta Geotech.* 12 (5): 971–986. https://doi.org/10.1007/s11440-017-0574-9.

Cundall, P. A., and O. D. L. Strack. 1979. "A discrete numerical model for granular assemblies." *Geotechnique* 29 (1): 47–65. https://doi.org/10.1680/geot.1979.29.1.47.

Dadda, A., C. Geindreau, F. Emeriault, S. R. du Roscoat, A. E. Filet, and A. Garandet. 2019. "Characterization of contact properties in biocemented sand using 3D X-ray micro-tomography." *Acta Geotech.* 14 (3): 597–613. https://doi.org/10.1007/s11440-018-0744-4.

Dadda, A., C. Geindreau, F. Emeriault, S. R. du Roscoat, A. Garandet, L. Sapin, and A. E. Filet. 2017. "Characterization of microstructural and physical properties changes in biocemented sand using 3D X-ray microtomography." *Acta Geotech.* 12 (5): 955–970. https://doi.org/10.1007/s11440-017-0578-5.

Darby, K. M., G. L. Hernandez, J. T. DeJong, R. W. Boulanger, M. G. Gomez, and D. W. Wilson. 2019. "Centrifuge model testing of liquefaction mitigation via microbially induced calcite precipitation." *J. Geotech. Geoenviron. Eng.* 145 (10): 04019084. https://doi.org/10.1061/(ASCE)GT.1943-5606.0002122.

DeJong, J. T., M. B. Fritzges, and K. Nüsslein. 2006. "Microbially induced cementation to control sand response to undrained shear." *J. Geotech. Geoenviron. Eng.* 132 (11): 1381–1392. https://doi.org/10.1061/(ASCE)1090-0241(2006)132:11(1381).

DeJong, J. T., B. M. Mortensen, B. C. Martinez, and D. C. Nelson. 2010. "Bio-mediated soil improvement." *Ecol. Eng.* 36: 197–210. https://doi.org/10.1016/j.ecoleng.2008.12.029.

DeJong, J. T., et al. 2013. "Biogeochemical processes and geotechnical applications: Progress, opportunities and challenges." *Géotechnique* 63 (4): 287–301. https://doi.org/10.1680/geot.SIP13.P.017.

Fattahi, S. M., A. Soroush, and N. Huang. 2020. "Biocementation control of sand against wind erosion." *J. Geotech. Geoenviron. Eng.* 146 (6): 04020045. https://doi.org/10.1061/(ASCE)GT.1943-5606.0002268.

Feng, K., and B. M. Montoya. 2017. "Quantifying level of microbial-induced cementation for cyclically loaded sand." *J. Geotech. Geoenviron. Eng.* 143 (6): 06017005. https://doi.org/10.1061/(ASCE)GT.1943-5606.0001682.

Gao, Y., L. Hang, J. He, and J. Chu. 2019. "Mechanical behaviour of biocemented sands at various treatment levels and relative densities." *Acta Geotech.* 14 (3): 697–707. https://doi.org/10.1007/s11440-018-0729-3.

Gomez, M. G., C. M. Anderson, C. M. R. Graddy, J. T. DeJong, D. C. Nelson, and T. R. Ginn. 2017. "Large-scale comparison of bioaugmentation and biostimulation approaches for biocementation of sands." *J. Geotech. Geoenviron. Eng.* 143 (5): 04016124. https://doi.org/10.1061/(ASCE)GT.1943-5606.0001640.

Gomez, M. G., J. T. DeJong, and C. M. Anderson. 2018. "Effect of bio-cementation on geophysical and cone penetration measurements in sands." *Can. Geotech. J.* 55 (11): 1632–1646. https://doi.org/10.1139/cgj-2017-0253.

Gomez, M. G., C. E. Hunt, B. C. Martinez, J. T. Dejong, D. W. Major, and S. M. Dworatzek. 2015. "Field-scale bio-cementation tests to improve sands." *Proc. Inst. Civ. Eng. Ground Improv.* 168 (6): 206–216. https://doi.org/10.1680/grim.13.00052.

Ham, S.-M., A. Martinez, G. Han, and T.-H. Kwon. 2022. "Grain-scale tensile and shear strengths of glass beads cemented by MICP." *J. Geotech. Geoenviron. Eng.* 148 (9): 04022068. https://doi.org/10.1061/(ASCE)GT.1943-5606.0002863.

Harkes, M. P., L. A. van Paassen, J. L. Booster, V. S. Whiffin, and M. C. M. van Loosdrecht. 2010. "Fixation and distribution of bacterial activity in sand to induce carbonate precipitation for ground reinforcement." *Ecol. Eng.* 36 (2): 112–117. https://doi.org/10.1016/j.ecoleng.2009.01.004.

He, J., Y. Gao, Z. Gu, J. Chu, and L. Wang. 2020. "Characterization of crude bacterial urease for $CaCO_3$ precipitation and cementation of silty sand." *J. Mater. Civ. Eng.* 32 (5): 04020071. https://doi.org/10.1061/(ASCE)MT.1943-5533.0003100.

Irani, N., and M. Ghasemi. 2021. "Effect of scrap tyre on strength properties of untreated and lime-treated clayey sand." *Eur. J. Environ. Civ. Eng.* 25 (9): 1609–1626. https://doi.org/10.1080/19648189.2019.1585964.

Jiang, M. J., J. D. Liu, Y. G. Sun, and Z. Y. Yin. 2013. "Investigation into macroscopic and microscopic behaviors of bonded sands using distinct element method." *Soils Found.* 53 (6): 804–819. https://doi.org/10.1016/j.sandf.2013.10.001.

Jiang, M. J., Y. G. Sun, L. Q. Li, and H. H. Zhu. 2012. "Contact behavior of idealized granules bonded in two different interparticle distances: An experimental investigation." *Mech. Mater.* 55: 1–15. https://doi.org/10.1016/j.mechmat.2012.07.002.

Jiang, N.-J., and K. Soga. 2017. "The applicability of microbially induced calcite precipitation (MICP) for internal erosion control in gravel–sand mixtures." *Géotechnique* 67 (1): 42–55. https://doi.org/10.1680/jgeot.15.P.182.

Jiang, N.-J., K. Soga, and M. Kuo. 2017. "Microbially induced carbonate precipitation for seepage-induced internal erosion control in sand–clay mixtures." *J. Geotech. Geoenviron. Eng.* 143 (3): 04016100. https://doi.org/10.1061/(ASCE)GT.1943-5606.0001559.

Jiang, N.-J., C.-S. Tang, L.-Y. Yin, Y.-H. Xie, and B. Shi. 2019. "Applicability of microbial calcification method for sandy-slope surface erosion control." *J. Mater. Civ. Eng.* 31 (11): 04019250. https://doi.org/10.1061/(ASCE)MT.1943-5533.0002897.

Johnson, K. L., K. Kendall, and A. D. Roberts. 1971. "Surface energy and contact of elastic solids." *Proc. R. Soc. London, Ser. A* 324 (1558): 301–313. https://doi.org/10.1098/rspa.1971.0141.

Kularathna, S., W. Liang, T. Zhao, B. Chandra, J. Zhao, and K. Soga. 2021. "A semi-implicit material point method based on fractional-step method for saturated soil." *Int. J. Numer. Anal. Methods Geomech.* 45 (10): 1405–1436. https://doi.org/10.1002/nag.3207.

Lee, M., G. Gomez Michael, M. El Kortbawi, and K. Ziotopoulou. 2022. "Effect of light biocementation on the liquefaction triggering and post-triggering behavior of loose sands." *J. Geotech. Geoenviron. Eng.* 148 (1): 04021170. https://doi.org/10.1061/(ASCE)GT.1943-5606.0002707.

Lee, M. L., W. S. Ng, and Y. Tanaka. 2013. "Stress-deformation and compressibility responses of bio-mediated residual soils." *Ecol. Eng.* 60: 142–149. https://doi.org/10.1016/j.ecoleng.2013.07.034.

Liang, W., and J. Zhao. 2019. "Multiscale modeling of large deformation in geomechanics." *Int. J. Numer. Anal. Methods Geomech.* 43 (5): 1080–1114. https://doi.org/10.1002/nag.2921.

Lin, H., M. T. Suleiman, D. G. Brown, and E. Kavazanjian Jr. 2016. "Mechanical behavior of sands treated by microbially induced carbonate precipitation." *J. Geotech. Geoenviron. Eng.* 142 (2): 04015066. https://doi.org/10.1061/(ASCE)GT.1943-5606.0001383.

Liu, K.-W., N.-J. Jiang, J.-D. Qin, Y.-J. Wang, C.-S. Tang, and X.-L. Han. 2021. "An experimental study of mitigating coastal sand dune erosion by microbial- and enzymatic-induced carbonate precipitation." *Acta Geotech.* 16 (2): 467–480. https://doi.org/10.1007/s11440-020-01046-z.

Liu, L., H. Liu, A. W. Stuedlein, T. M. Evans, and Y. Xiao. 2019. "Strength, stiffness, and microstructure characteristics of biocemented calcareous sand." *Can. Geotech. J.* 56 (10): 1502–1513. https://doi.org/10.1139/cgj-2018-0007.

Liu, S., and X. Gao. 2020. "Evaluation of the anti-erosion characteristics of an MICP coating on the surface of tabia." *J. Mater. Civ. Eng.* 32 (10): 04020304. https://doi.org/10.1061/(ASCE)MT.1943-5533.0003408.

Ma, G., X. He, X. Jiang, H. Liu, J. Chu, and Y. Xiao. 2021. "Strength and permeability of bentonite-assisted biocemented coarse sand." *Can. Geotech. J.* 57 (7): 969–981. https://doi.org/10.1139/cgj-2020-0045.

Ma, G., Y. Xiao, X. He, J. Li, J. Chu, and H. Liu. 2022. "Kaolin-nucleation-based biotreated calcareous sand through unsaturated percolation method." *Acta Geotech.* 17: 3181–3193. https://doi.org/10.1007/s11440-022-01459-y.

Mahawish, A., A. Bouazza, and W. P. Gates. 2019. "Unconfined compressive strength and visualization of the microstructure of coarse sand subjected to different biocementation levels." *J. Geotech. Geoenviron. Eng.* 145 (8): 04019033. https://doi.org/10.1061/(ASCE)GT.1943-5606.0002066.

Martinez, A., L. Huang, and M. G. Gomez. 2019. "Thermal conductivity of MICP-treated sands at varying degrees of saturation." *Geotech. Lett.* 9 (1): 15–21. https://doi.org/10.1680/jgele.18.00126.

Martinez, B. C., J. T. DeJong, T. R. Ginn, B. M. Montoya, T. H. Barkouki, C. Hunt, B. Tanyu, and D. Major. 2013. "Experimental optimization of microbial-induced carbonate precipitation for soil improvement." *J. Geotech. Geoenviron. Eng.* 139 (4): 587–598. https://doi.org/10.1061/(ASCE)GT.1943-5606.0000787.

Montoya, B. M., and J. T. DeJong. 2015. "Stress–strain behavior of sands cemented by microbially induced calcite precipitation." *J. Geotech. Geoenviron. Eng.* 141 (6): 04015019. https://doi.org/10.1061/(ASCE)GT.1943-5606.0001302.

Montoya, B. M., J. T. DeJong, and R. W. Boulanger. 2013. "Dynamic response of liquefiable sand improved by microbial-induced calcite precipitation." *Géotechnique* 63 (4): 302–312. https://doi.org/10.1680/geot.SIP13.P.019.

Montoya, B. M., J. Do, and M. A. Gabr. 2021. "Distribution and properties of microbially induced carbonate precipitation in underwater sand bed." *J. Geotech. Geoenviron. Eng.* 147 (10): 04021098. https://doi.org/10.1061/(ASCE)GT.1943-5606.0002607.

Montoya, B. M., S. Safavizadeh, and M. A. Gabr. 2019. "Enhancement of coal ash compressibility parameters using microbial-induced carbonate precipitation." *J. Geotech. Geoenviron. Eng.* 145 (5): 04019018. https://doi.org/10.1061/(ASCE)GT.1943-5606.0002036.

Mortensen, B. M., M. J. Haber, J. T. DeJong, L. F. Caslake, and D. C. Nelson. 2011. "Effects of environmental factors on microbial induced calcium carbonate precipitation." *J. Appl. Microbiol.* 111 (2): 338–349. https://doi.org/10.1111/j.1365-2672.2011.05065.x.

Mousavi, S., and M. Ghayoomi. 2021. "Liquefaction mitigation of sands with nonplastic fines via microbial-induced partial saturation." *J. Geotech. Geoenviron. Eng.* 147 (2): 04020156. https://doi.org/10.1061/(ASCE)GT.1943-5606.0002444.

Nafisi, A., D. Mocelin, B. M. Montoya, and S. Underwood. 2019. "Tensile strength of sands treated with microbially induced carbonate precipitation." *Can. Geotech. J.* 57 (10): 1611–1616. https://doi.org/10.1139/cgj-2019-0230.

Nassar, M. K., D. Gurung, M. Bastani, T. R. Ginn, B. Shafei, M. G. Gomez, C. M. R. Graddy, D. C. Nelson, and J. T. DeJong. 2018. "Large-scale experiments in microbially induced calcite precipitation (MICP): Reactive transport model development and prediction." *Water Resour. Res.* 54 (1): 480–500. https://doi.org/10.1002/2017wr021488.

Pan, X., J. Chu, Y. Yang, and L. Cheng. 2020. "A new biogrouting method for fine to coarse sand." *Acta Geotech.* 15 (1): 1–16. https://doi.org/10.1007/s11440-019-00872-0.

Pham, V. P., L. A. van Paassen, W. R. L. van der Star, and T. J. Heimovaara. 2018. "Evaluating strategies to improve process efficiency of denitrification-based MICP." *J. Geotech. Geoenviron. Eng.* 144 (8): 04018049. https://doi.org/10.1061/(ASCE)GT.1943-5606.0001909.

Proto, C. J., J. T. DeJong, and D. C. Nelson. 2016. "Biomediated permeability reduction of saturated sands." *J. Geotech. Geoenviron. Eng.* 142 (12): 04016073. https://doi.org/10.1061/(ASCE)GT.1943-5606.0001558.

Rahmannejad, M., and V. Toufigh. 2018. "Influence of curing time and water content on unconfined compressive strength of sand stabilized using epoxy resin." *Int. J. Eng.* 31 (8): 1187–1195. https://doi.org/10.5829/ije.2018.31.08b.05.

Ren, J., H. He, and K. Senetakis. 2021. "A micromechanical-based investigation on the frictional behaviour of artificially bonded analogue sedimentary rock with calcium carbonate." *Pure Appl. Geophys.* 178: 4461–4486. https://doi.org/10.1007/s00024-021-02875-z.

Riveros, G. A., and A. Sadrekarimi. 2020. "Effect of microbially induced cementation on the instability and critical state behaviours of Fraser River sand." *Can. Geotech. J.* 57 (12): 1870–1880. https://doi.org/10.1139/cgj-2019-0514.

San Pablo, A. C. M., et al. 2020. "Meter-scale biocementation experiments to advance process control and reduce impacts: Examining spatial control, ammonium by-product removal, and chemical reductions." *J. Geotech. Geoenviron. Eng.* 146 (11): 04020125. https://doi.org/10.1061/(ASCE)GT.1943-5606.0002377.

Sasaki, T., and R. Kuwano. 2016. "Undrained cyclic triaxial testing on sand with non-plastic fines content cemented with microbially induced $CaCO_3$." *Soils Found.* 56 (3): 485–495. https://doi.org/10.1016/j.sandf.2016.04.014.

Sharma, M., N. Satyam, and K. R. Reddy. 2021. "Effect of freeze–thaw cycles on engineering properties of biocemented sand under different treatment conditions." *Eng. Geol.* 284: 106022. https://doi.org/10.1016/j.enggeo.2021.106022.

Soon, N. W., L. M. Lee, T. C. Khun, and H. S. Ling. 2014. "Factors affecting improvement in engineering properties of residual soil through microbial-induced calcite precipitation." *J. Geotech. Geoenviron. Eng.* 140 (5): 04014006. https://doi.org/10.1061/(ASCE)GT.1943-5606.0001089.

Stocks-Fischer, S., J. K. Galinat, and S. S. Bang. 1999. "Microbiological precipitation of $CaCO_3$." *Soil Biol. Biochem.* 31 (11): 1563–1571. https://doi.org/10.1016/s0038-0717(99)00082-6.

Sun, X., L. Miao, R. Chen, H. Wang, L. Wu, and J. Xia. 2021a. "Liquefaction resistance of biocemented loess soil." *J. Geotech. Geoenviron. Eng.* 147 (11): 04021117. https://doi.org/10.1061/(ASCE)GT.1943-5606.0002638.

Sun, X., L. Miao, J. Xia, and H. Wang. 2021b. "Evaluation and prediction for the cementation effect of MICP based on electrical resistivity." *J. Mater. Civ. Eng.* 33 (10): 06021006. https://doi.org/10.1061/(ASCE)MT.1943-5533.0003896.

Terzis, D., and L. Laloui. 2019. "Cell-free soil bio-cementation with strength, dilatancy and fabric characterization." *Acta Geotech.* 14 (3): 639–656. https://doi.org/10.1007/s11440-019-00764-3.

Toohey, N. M., M. A. Mooney, and R. G. Bearce. 2013. "Relationship between resilient modulus and unconfined compressive strength for lime-stabilized soils." *J. Geotech. Geoenviron. Eng.* 139 (11): 1982–1985. https://doi.org/10.1061/(ASCE)GT.1943-5606.0000925.

van Paassen, L. A., C. M. Daza, M. Staal, D. Y. Sorokin, W. van der Zon, and M. C. M. van Loosdrecht. 2010a. "Potential soil reinforcement by biological denitrification." *Ecol. Eng.* 36: 168–175. https://doi.org/10.1016/j.ecoleng.2009.03.026.

van Paassen, L. A., R. Ghose, T. J. M. van der Linden, W. R. L. van der Star, and M. C. M. van Loosdrecht. 2010b. "Quantifying biomediated ground improvement by ureolysis: Large-scale biogrout experiment." *J. Geotech. Geoenviron. Eng.* 136 (12): 1721–1728. https://doi.org/10.1061/(ASCE)GT.1943-5606.0000382.

Venda Oliveira, P. J., M. S. da Costa, J. N. P. Costa, and M. F. Nobre. 2015. "Comparison of the ability of two bacteria to improve the behavior of sandy soil." *J. Mater. Civ. Eng.* 27 (1): 06014025. https://doi.org/10.1061/(ASCE)MT.1943-5533.0001138.

Venuleo, S., L. Laloui, D. Terzis, T. Hueckel, and M. Hassan. 2016. "Microbially induced calcite precipitation effect on soil thermal conductivity." *Geotech. Lett.* 6 (1): 39–44. https://doi.org/10.1680/jgele.15.00125.

Wang, J., Y. Zhou, T. Wu, and X. Wu. 2019a. "Performance of cement asphalt mortar in ballastless slab track over high-speed railway under extreme climate conditions." *Int. J. Geomech.* 19 (5): 04019037. https://doi.org/10.1061/(ASCE)GM.1943-5622.0001419.

Wang, W., V. Nardelli, and M. R. Coop. 2017. "Micro-mechanical behaviour of artificially cemented sands under compression and shear." *Geotech. Lett.* 7 (3): 218–224. https://doi.org/10.1680/jgele.16.00166.

Wang, W. Y., M. R. Coop, and K. Senetakis. 2019b. "The development of a micromechanical apparatus applying combined normal-shear-bending forces to natural sand grains with artificial bonds." *Geotech. Test. J.* 42 (4): 1090–1099. https://doi.org/10.1520/gtj20170453.

Wang, X. R., J. L. Tao, R. T. Bao, T. Tran, and S. Tucker-Kulesza. 2018. "Surficial soil stabilization against water-induced erosion using polymer-modified microbially induced carbonate precipitation." *J. Mater. Civ. Eng.* 30 (10): 04018267. https://doi.org/10.1061/(ASCE)MT.1943-5533.0002490.

Wang, Y., K. Soga, J. T. DeJong, and A. J. Kabla. 2019c. "A microfluidic chip and its use in characterising the particle-scale behaviour of microbial-induced calcium carbonate precipitation (MICP)." *Geotechnique* 69 (12): 1086–1094. https://doi.org/10.1680/jgeot.18.P.031.

Wang, Y., K. Soga, J. T. DeJong, and A. J. Kabla. 2019d. "Microscale visualization of microbial-induced calcium carbonate precipitation processes." *J. Geotech. Geoenviron. Eng.* 145 (9): 04019045. https://doi.org/10.1061/(ASCE)GT.1943-5606.0002079.

Wang, Y., K. Soga, J. T. DeJong, and A. J. Kabla. 2021. "Effects of bacterial density on growth rate and characteristics of microbial-induced $CaCO_3$ precipitates: Particle-scale experimental study." *J. Geotech. Geoenviron. Eng.* 147 (6): 04021036. https://doi.org/10.1061/(ASCE)GT.1943-5606.0002509.

Wang, Y. H., and S. C. Leung. 2008. "A particulate-scale investigation of cemented sand behavior." *Can. Geotech. J.* 45 (1): 29–44. https://doi.org/10.1139/t07-070.

Wang, Z., L. Li, L. Song, S. Guo, and Q. Dai. 2019e. "High-frequency fatigue performance of cracked mortar after epoxy grouting reinforcement." *Int. J. Geomech.* 19 (5): 04019035. https://doi.org/10.1061/(ASCE)GM.1943-5622.0001416.

Wang, Z., N. Zhang, J. Ding, Q. Li, and J. Xu. 2020. "Thermal conductivity of sands treated with microbially induced calcite precipitation (MICP) and model prediction." *Int. J. Heat Mass Transfer* 147: 118899. https://doi.org/10.1016/j.ijheatmasstransfer.2019.118899.

Wen, K., Y. Li, S. Liu, C. Bu, and L. Li. 2019. "Development of an improved immersing method to enhance microbial induced calcite precipitation treated sandy soil through multiple treatments in low cementation media concentration." *Geotech. Geol. Eng.* 37: 1015–1027. https://doi.org/10.1007/s10706-018-0669-6.

Whiffin, V. S., L. A. van Paassen, and M. P. Harkes. 2007. "Microbial carbonate precipitation as a soil improvement technique." *Geomicrobiol. J.* 24 (5): 417–423. https://doi.org/10.1080/01490450701436505.

Wu, H., N. Guo, and J. Zhao. 2018. "Multiscale modeling and analysis of compaction bands in high-porosity sandstones." *Acta Geotech.* 13 (3): 575–599. https://doi.org/10.1007/s11440-017-0560-2.

Xiao, P., H. Liu, A. W. Stuedlein, T. M. Evans, and Y. Xiao. 2019a. "Effect of relative density and biocementation on the cyclic response of calcareous sand." *Can. Geotech. J.* 56 (12): 1849–1862. https://doi.org/10.1139/cgj-2018-0573.

Xiao, P., H. Liu, Y. Xiao, A. W. Stuedlein, and T. M. Evans. 2018. "Liquefaction resistance of bio-cemented calcareous sand." *Soil Dyn. Earthquake Eng.* 107: 9–19. https://doi.org/10.1016/j.soildyn.2018.01.008.

Xiao, Y., H. Chen, A. W. Stuedlein, T. M. Evans, J. Chu, L. Cheng, N. Jiang, H. Lin, H. Liu, and H. M. Aboel-Naga. 2020a. "Restraint of particle breakage by biotreatment method." *J. Geotech. Geoenviron. Eng.* 146 (11): 04020123. https://doi.org/10.1061/(ASCE)GT.1943-5606.0002384.

Xiao, Y., X. He, T. M. Evans, A. W. Stuedlein, and H. Liu. 2019b. "Unconfined compressive and splitting tensile strength of basalt fiber-reinforced biocemented sand." *J. Geotech. Geoenviron. Eng.* 145 (9): 04019048. https://doi.org/10.1061/(ASCE)GT.1943-5606.0002108.

Xiao, Y., X. He, A. W. Stuedlein, J. Chu, T. M. Evans, and L. A. van Paassen. 2022a. "Crystal growth of MICP through microfluidic chip tests." *J. Geotech. Geoenviron. Eng.* 148 (5): 06022002. https://doi.org/10.1061/(ASCE)GT.1943-5606.0002756.

Xiao, Y., X. He, W. Wu, A. Stuedlein, W. T, M. Evans, J. Chu, H. Liu, L. A. van Paassen, and H. Wu. 2021a. "Kinetic biomineralization through microfluidic chip tests." *Acta Geotech.* 16 (10): 3229–3237. https://doi.org/10.1007/s11440-021-01205-w.

Xiao, Y., X. He, M. Zaman, G. Ma, and C. Zhao. 2022b. "Review of strength improvements of biocemented soils." *Int. J. Geomech.* 22 (11): 03122001. https://doi.org/10.1061/(ASCE)GM.1943-5622.0002565.

Xiao, Y., G. Ma, H. Wu, H. Lu, and M. Zaman. 2022c. "Rainfall-induced erosion of biocemented graded slopes." *Int. J. Geomech.* 22 (1): 04021256. https://doi.org/10.1061/(ASCE)GM.1943-5622.0002239.

Xiao, Y., A. W. Stuedlein, Z. Pan, H. Liu, T. M. Evans, X. He, H. Lin, J. Chu, and L. A. van Paassen. 2020b. "Toe-bearing capacity of precast concrete piles through biogrouting improvement." *J. Geotech. Geoenviron. Eng.* 146 (12): 06020026. https://doi.org/10.1061/(ASCE)GT.1943-5606.0002404.

Xiao, Y., A. W. Stuedlein, J. Ran, T. M. Evans, L. Cheng, H. Liu, L. A. van Paassen, and J. Chu. 2019c. "Effect of particle shape on strength and stiffness of biocemented glass beads." *J. Geotech. Geoenviron. Eng.* 145 (11): 06019016. https://doi.org/10.1061/(ASCE)GT.1943-5606.0002165.

Xiao, Y., Y. Tang, G. Ma, J. S. McCartney, and J. Chu. 2021b. "Thermal conductivity of biocemented graded sands." *J. Geotech. Geoenviron. Eng.* 147 (10): 04021106. https://doi.org/10.1061/(ASCE)GT.1943-5606.0002621.

Xiao, Y., W. Xiao, G. Ma, X. He, H. Wu, and J. Shi. 2022d. "Mechanical performance of biotreated sandy road bases." *J. Perform. Constr. Facil.* 36 (1): 04021111. https://doi.org/10.1061/(ASCE)CF.1943-5509.0001671.

Xiao, Y., Z. Yuan, J. Lin, J. Ran, B. Dai, J. Chu, and H. Liu. 2019d. "Effect of particle shape of glass beads on the strength and deformation of cemented sands." *Acta Geotech.* 14 (6): 2123–2131. https://doi.org/10.1007/s11440-019-00830-w.

Xiao, Y., Z. Zhang, A. W. Stuedlein, and T. M. Evans. 2021c. "Liquefaction modeling for biocemented calcareous sand." *J. Geotech. Geoenviron. Eng.* 147 (12): 04021149. https://doi.org/10.1061/(ASCE)GT.1943-5606.0002666.

Xiao, Y., C. Zhao, Y. Sun, S. Wang, H. Wu, H. Chen, and H. Liu. 2021d. "Compression behavior of MICP-treated sand with various gradations." *Acta Geotech.* 16 (5): 1391–1400. https://doi.org/10.1007/s11440-020-01116-2.

Xiao, Y., W. Zhou, J. Shi, H. Lu, and Z. Zhang. 2022e. "Erosion of biotreated field-scale slopes under rainfalls." *J. Perform. Constr. Facil.* 36 (3): 04022030. https://doi.org/10.1061/(ASCE)CF.1943-5509.0001732.

Yang, Y., J. Chu, Y. Xiao, H. Liu, and L. Cheng. 2019. "Seepage control in sand using bioslurry." *Constr. Build. Mater.* 212: 342–349. https://doi.org/10.1016/j.conbuildmat.2019.03.313.

Zamani, A., and B. M. Montoya. 2018. "Undrained monotonic shear response of MICP-treated silty sands." *J. Geotech. Geoenviron. Eng.* 144 (6): 04018029. https://doi.org/10.1061/(ASCE)GT.1943-5606.0001861.

Zamani, A., and B. M. Montoya. 2019. "Undrained cyclic response of silty sands improved by microbial induced calcium carbonate precipitation." *Soil Dyn. Earthquake Eng.* 120: 436–448. https://doi.org/10.1016/j.soildyn.2019.01.010.

Zamani, A., P. Xiao, T. Baumer, T. J. Carey, B. Sawyer, J. T. DeJong, and R. W. Boulanger. 2021. "Mitigation of liquefaction triggering and foundation settlement by MICP treatment." *J. Geotech. Geoenviron. Eng.* 147 (10): 04021099. https://doi.org/10.1061/(ASCE)GT.1943-5606.0002596.

Zhao, Q., L. Li, C. Li, M. Li, F. Amini, and H. Zhang. 2014. "Factors affecting improvement of engineering properties of MICP-treated soil catalyzed by bacteria and urease." *J. Mater. Civ. Eng.* 26 (12): 04014094. https://doi.org/10.1061/(ASCE)MT.1943-5533.0001013.

Zhao, S., J. Zhao, and W. Liang. 2021. "A thread-block-wise computational framework for large-scale hierarchical continuum-discrete modeling of granular media." *Int. J. Numer. Methods Eng.* 122 (2): 579–608. https://doi.org/10.1002/nme.6549.

Zhao, S., J. Zhao, W. Liang, and F. Niu. 2022. "Multiscale modeling of coupled thermo-mechanical behavior of granular media in large deformation and flow." *Comput. Geotech.* 149: 104855. https://doi.org/10.1016/j.compgeo.2022.104855.